nature

https://doi.org/10.1038/s41586-022-05541-z

Accelerated Article Preview

Regulating surface potential maximizes voltage in all-perovskite tandems

Received: 24 June 2022

Accepted: 8 November 2022

Accelerated Article Preview
Published online: 15 November 2022

Cite this article as: Chen, H. et al. Regulating surface potential maximizes voltage in all-perovskite tandems. *Nature* https://doi.org/10.1038/s41586-022-05541-z (2022)

Hao Chen, Aidan Maxwell, Chongwen Li, Sam Teale, Bin Chen, Tong Zhu, Esma Ugur, George Harrison, Luke Grater, Junke Wang, Zaiwei Wang, Lewei Zeng, So Min Park, Lei Chen, Peter Serles, Rasha Abbas Awni, Biwas Subedi, Xiaopeng Zheng, Chuanxiao Xiao, Nikolas J. Podraza, Tobin Filleter, Cheng Liu, Yi Yang, Joseph M. Luther, Stefaan De Wolf, Mercouri G. Kanatzidis, Yanfa Yan & Edward H. Sargent

Title: Regulating surface potential maximizes voltage in all-perovskite tandems

Authors: *Hao Chen,[1,†] Aidan Maxwell,[1,†] Chongwen Li,[1,2,†] Sam Teale,[1,†] Bin Chen,[1,3†] Tong Zhu,[1] Esma Ugur,[4] George Harrison,[4] Luke Grater,[1] Junke Wang,[1] Zaiwei Wang,[1] Lewei Zeng,[1] So Min Park,[1] Lei Chen,[2] Peter Serles,[5] Rasha Abbas Awni,[2] Biwas Subedi,[2] Xiaopeng Zheng,[6] Chuanxiao Xiao,[6] Nikolas J. Podraza,[2] Tobin Filleter,[4] Cheng Liu,[3,7] Yi Yang,[3,7] Joseph M. Luther,[6] Stefaan De Wolf,[4] Mercouri G. Kanatzidis,[3] Yanfa Yan,[2*] Edward H. Sargent[1,3,7*]*

Affiliations:

[1] The Edward S. Rogers Department of Electrical and Computer Engineering, University of Toronto, Toronto, Ontario M5S 3G4, Canada

[2] Department of Physics and Astronomy and Wright Center for Photovoltaics Innovation and Commercialization, The University of Toledo, Toledo, Ohio 43606, USA

[3] Department of Chemistry, Northwestern University, Evanston, Illinois 60208, United States

[4] KAUST Solar Center (KSC), Physical Sciences and Engineering Division (PSE), King Abdullah University of Science and Technology (KAUST), Thuwal 23955-6900, Kingdom of Saudi Arabia

[5] Department of Mechanical and Industrial Engineering, University of Toronto, 5 King's College Road, Toronto, Ontario M5S 3G8, Canada

[6] National Renewable Energy Laboratory, Golden, Colorado 80401, USA

[7] Department of Electrical and Computer Engineering, Northwestern University, Evanston, Illinois 60208, United States

*Correspondence to: ted.sargent@utoronto.ca, yanfa.yan@utoledo.edu

†These authors contributed equally

Abstract:

The open circuit voltage (V_{OC}) deficit in perovskite solar cells (PSCs) is greater in wide bandgap (>1.7 eV) cells than in ~1.5 eV perovskites.[1,2] Quasi-Fermi level splitting (QFLS) measurements reveal V_{OC}-limiting recombination at the electron transport layer (ETL) contact.[3-5] This, we find, stems from inhomogeneous surface potential and poor perovskite-ETL energetic alignment. Common monoammonium surface treatments fail to address this; instead we introduce diammonium molecules to modify the perovskite surface states and achieve a more uniform spatial distribution of surface potential. Using 1,3-propane diammonium (PDA), QFLS increases by 90 meV, enabling 1.79 eV PSCs with a certified 1.33 V V_{OC}, and > 19% power conversion efficiency (PCE). Incorporating this layer into a monolithic all-perovskite tandem, we report a record V_{OC} of 2.19 V (89% of the detailed balance V_{OC} limit) and > 27% PCE (26.3% certified quasi-steady-state). These tandems retain more than 86% of their initial PCE after 500 hrs operation.

Main Text:

The wide range of bandgaps achievable using metal-halide perovskites (~ 1.2 eV – 3.0 eV) has enabled tandem solar cells with silicon, copper indium gallium selenide (CIGS), and organic photovoltaics.[6-9] Recently, all-perovskite tandems made from stacked wide-bandgap (WBG) ~1.8 eV and narrow-bandgap (NBG) ~1.2 eV layers surpassed the highest recorded power conversion efficiency (PCE) for a single-junction perovskite solar cell (PSC).[10,11]

Despite rapid progress, the PCE of perovskite tandems is limited by the large open-circuit voltage (V_{OC}) loss of the WBG cell.[1,2] While single-junction ~ 1.5 eV PSCs have demonstrated V_{OC} deficits (the difference between the bandgap and device V_{OC}) as low as 0.3 V,[12] mixed iodide/bromide >1.75 eV PSCs have yet to achieve V_{OC} deficits lower than 0.5 V (Supplementary Fig. S1).[13,14] The V_{OC} deficit has been suggested to stem from increased trap density in perovskites with > 20% Br concentration, photoinduced halide segregation, and poor energetic alignment with charge transport layers.[15,16] The photoluminescence quantum yield (PLQY) of perovskites, once in contact with charge transport layers, tends to decrease dramatically, suggesting that the perovskite/transport-layer interface produces recombination pathways within the perovskite bandgap.[3-5] Several causes have been reported in efforts to uncover the origin of this phenomenon: band misalignment,[16] energy-level pinning,[5] and halide migration from the perovskite into the transport layer.[17] Here we examine the perovskite/C_{60} interface as it is ubiquitous in perovskite tandems, is the most easily accessed interface when fabricating inverted (*pin*) PSCs, and yet remains to be considered one of the worst offenders for inducing trap states.[16,5]

We spin-coated WBG perovskite $Cs_{0.2}FA_{0.8}Pb(I_{0.6}Br_{0.4})_3$ films atop ITO/hole transport layer (HTL) substrates with a structure of ITO/NiOx/Me-4PACz and measured their PLQY with and without a C_{60} layer (Fig. 1b). Consistent with previous reports,[3,5] we found that after C_{60} deposition, the PLQY is two orders of magnitude lower, equivalent to a drop of ~100 meV in quasi-Fermi level splitting (QFLS).[18]

Previous studies have focused on post-treatments which reduce the defect density of the perovskite surface, and thus increase the PLQY of films.[19–22] Extending this practice to WBG perovskites we found that treating the surface with the popular passivant butylammonium iodide (BA) increases PLQY, but that the improvement is not retained following the deposition of C_{60} (Fig. 1b). Indeed, the QFLS of the stack is likely pinned due to interfacial recombination rather than the inherent trap density of the perovskite.[5]

Seeking a different approach, we reasoned that tuning the surface potential at the perovskite/C_{60} interface would suppress this cross-interface recombination by reducing the band offset between the perovskite and C_{60}, and reducing the population of minority carriers at the interface. This effect is analogous to field-effect passivation in traditional Si solar cells.[23,24] Thus, we turned our focus toward short-chain diammonium ligands, strong Lewis bases that have previously been shown to induce n-type doping and surface dipoles which alter surface energetics in mixed Pb-Sn perovskites.[25–27] Treating the perovskite surface with 1,3-propane-diammonium iodide (PDA) (Fig. 1a), the diammonium equivalent to BA, we observed only a slight increase in PLQY. However, following deposition of C_{60} there was no dramatic drop in PLQY, suggesting that the recombination pathways induced by the C_{60} had been effectively suppressed. We also compared the effects of perovskite post-treatments with similar concentrations of 1,2-ethane-diammonium iodide (EDA) and 1,4-butane-diammonium iodide (BDA), diammonium ligands with a shorter and longer chain length, respectively. Of these diammonium ligands, only PDA resulted in the retention of PLQY after the deposition of C_{60} (Supplementary Fig. S3).

To understand how both treatments affect interface energetics we used ultra-violet photoelectron spectroscopy (UPS) and found that BA induces a Fermi level downshift, whereas PDA induces a Fermi level upshift, resulting in stronger and weaker surface p-type doping, respectively (Fig. 1c). The latter change in the surface potential produces a lower minority carrier concentration at the interface and it reduces the band offset between the perovskite and C_{60} by 60 meV. Drift-diffusion modelling suggests that this has the potential to increase QFLS by ~ 90 meV (Supplementary Fig. S4).

Using time of flight secondary ion mass spectrometry (ToF-SIMS) and X-ray photoelectron spectroscopy (XPS) (Supplementary Fig. S5, S6) we found that PDA ligands are present on the film surface after treatment. Using density functional theory, we studied the work function changes upon PDA treatment of various surface structures (Supplementary Fig. S7, Fig. 1d). Among considered surface configurations that we contemplated, the pristine Pb-I terminated surface with a bromide vacancy (V_{Br}), which exhibited a 0.44 eV lower work function after PDA treatment (Supplementary Fig. S8), was in best agreement with the 0.1 eV shift obtained from the experimental UPS data. Then, through density of states (DOS) analysis of BA and PDA surface treatments (Fig. 1e, Supplementary Fig. S9), we found that after PDA treatment, the in-gap surface states near the valence band maximum (VBM) region are suppressed (see supplementary materials), consistent with the Fermi level upshift relative to the VBM (Fig. 1c) observed in UPS measurements.

Seeking to investigate how PDA affects films on the nanoscale, we used hyperspectral imaging to generate QFLS maps of perovskite films with and without C_{60} (Fig. 2a-b, Supplementary Fig. S10). From these maps we observe significantly greater spatial fluctuation than has been observed for perovskites with narrower bandgaps (< 1.65 eV) which have a typical standard deviation (σ) in QFLS of ~ 10 meV.[4,28] After PDA treatment, however, σ lowers significantly (61 meV to 24 meV), suggesting the treated film is more homogeneous. After C_{60} deposition the QFLS of the control drops (1.32 to 1.25 eV) and broadens further (σ = 77 meV), whereas the QFLS of the PDA film is retained at 1.33 eV with a slightly narrower distribution (σ = 22 meV). Kelvin probe force microscopy (KPFM) (Fig. 2c-d, Supplementary Fig. S11) suggests that this effect is correlated with the nonuniform contact potential of the control film, which will act to broaden the interfacial electronic states when in contact with C_{60} leading to increased recombination.[5,29] PDA treatment narrows the contact potential distribution significantly (σ = 2.9 mV compared to 11.1 mV for the control), which is indicative of reduced recombination and improved carrier extraction.[30,31]

We used grazing incidence wide-angle X-ray scattering (GIWAXS) to reveal the crystallographic consequences of PDA treatment. Varying the incident angle of the X-ray beam, we compared the crystal structure of the film bulk (1°) and surface (0.15°) (Fig. 2e-h, Supplementary Fig. S12). In contrast to prior perovskite systems treated with diammonium ligands, there exist no low-q-value peaks for the PDA treated film: thus, no indication of reduced-dimensional perovskite formation,[32,33] nor of a perovskite polymorph.[34] The concentration of PDA spin-coated onto the perovskite surface is low and thus does not appear to result in appreciable diffusion into the bulk perovskite. Two structural differences between control and treated films are apparent however: a peak at 0.88 $Å^{-1}$ for the control which we ascribe to PbI_2, which is entirely removed by PDA, and a secondary peak with a q-space value of 1.03 $Å^{-1}$ alongside the (1 1 0) perovskite peak (1.00 $Å^{-1}$), indicative of a Br-rich phase. This secondary peak is more obvious when probing only the first ~ 5 nm of film, suggesting that the film surface is segregated into PbI_2 and Br-rich perovskite regions, the likely cause of the broad contact potential.[35] The suppression of surface phase segregation and removal of PbI_2 implies that while PDA does not induce the formation of a new crystal phase, it does react with the surface of the perovskite. This has been observed previously with diammoniums which template the growth of perovskite crystallization.[36,37] This is corroborated by SEM images (Supplementary Fig. S13), transient absorption (Supplementary Fig. S14) and transient reflection (TR) spectra (Fig. 2i, j). The TR spectra reveal that two additional bleaches are present in the control compared to the PDA treated sample: a peak around 500 nm (PbI_2) and a fast-decaying bleach at around 600 nm (~ 85% Br-rich perovskite, which correlates exactly with the shift in q-space seen in GIWAXS).[38]

Encouraged by the reduced interfacial recombination and surface homogeneity imparted by the PDA treatment, we fabricated WBG solar cells. The device structure was ITO/NiOx/Me-4PACz/perovskite/C_{60}/ALD-SnOx/Ag, where Me-4PACz is a self-assembled monolayer of [4-(3,6-Dimethyl-9H-carbazol-9-yl)butyl]phosphonic acid. Fig. 3a contains the forward and reverse *J-V* curves for champion control and PDA-treated 1.79 eV WBG PSCs (EQE spectrum shown in Supplementary Fig. S15), exhibiting a V_{OC} increase from 1.23 to 1.33 V, the highest V_{OC} reported for ~ 1.8 eV PSCs (Supplementary

Fig. S1). Fig. 3b shows the *J-V* curve of a PDA-treated PSC exhibiting a V_{OC} of ~1.33 V and a PCE of 19.3% as verified by the PV cell and module performance group at the National Renewable Energy Lab (NREL) (Supplementary Fig. S16). Improvements in device V_{OC}, FF and PCE were consistent across 30 control and PDA-treated devices, as shown in Fig. 3c. We also fabricated 1 cm^2 WBG devices using the PDA surface treatment, which delivered a V_{OC} of ~1.35 V and a PCE of 19.0% (Supplementary Fig. S17).

We conducted transient photovoltage and photocurrent (TPV/C) measurements of control and PDA-treated devices (Supplementary Fig. S19). The charge-recombination lifetime (τ_r) of the PDA-treated device was longer than that of the control device (2.0 μs compared to 0.4 μs), consistent with reduced carrier trapping at the C_{60} interface after PDA post-treatment (Supplementary Fig. S20, Supplementary Table S4).[39] Calculating the diffusion length (see Supplementary Note 2), we found that PDA treatment results in a 2-fold increase, from 600 nm to 1.2 μm.

We followed the output of a PDA-treated WBG cell operating for 700 hrs at the maximum power point (MPP) to determine the impact of PDA on device stability (Supplementary Fig. S21). After 700 hours of continuous operation under 1-sun illumination, the PDA-treated device exhibited no loss in PCE. We attribute this to an increased ion migration barrier exhibited in the PDA treated films, calculated from thermal admittance spectroscopy (Supplementary Fig. S22).

We used intensity-dependent PLQY measurements to conduct systematic loss analysis (See Pseudo-*JV* Methods) of control vs. PDA treated films (Fig. 3d, Supplementary Table S3).[40] Both samples have similar bulk and HTL interface losses, but the PDA treatment reduces V_{OC} loss at the ETL from 104 mV to 16 mV. PDA also eliminates a 14 mV mismatch between the full stack QFLS and device V_{OC} present in the control sample, indicating a reduced band offset between perovskite and C_{60} after treatment,[16] consistent with band alignment analysis in Fig. 1. In addition to reduced V_{OC} loss, PDA treated devices exhibit reduced transport (fill factor) losses compared to the control, $3.4\%_{abs.}$ vs. $8\%_{abs.}$ (Supplementary Table S3). This also suggests favorable band bending at the treated interface, resulting in improved carrier extraction.

Using our high-V_{OC} PDA-treated WBG active layer in combination with a $Cs_{0.05}FA_{0.7}MA_{0.25}Pb_{0.5}Sn_{0.5}I_3$ ~1.2 eV NBG mixed Pb-Sn perovskite, we fabricated monolithic all-perovskite tandem solar cells (see details in Methods). The tandem device structure was ITO/NiOx/Me-4PACz/WBG perovskite/C_{60}/ALD SnOx/Au (1 nm)/PEDOT:PSS/NBG perovskite/C_{60}/ALD SnOx/Ag (Fig. 4a), and the SEM cross-sectional image shows the ~1 μm thick Pb-Sn perovskite layer needed for current matching (Fig. 4b).[10] The integrated short-circuit current density (J_{SC}) values for the WBG and NBG subcells from EQE measurements of a tandem device were 15.4 and 15.2 mA/cm^2, respectively (Fig. 4c). The bandgaps of the WBG and NBG subcells calculated from the EQE spectra were 1.79 eV and 1.22 eV respectively.

Figure 4d shows forward and reverse *J-V* scans of a champion tandem, WBG and NBG PSCs. A record PCE of 27.4% was achieved with a high V_{OC} of 2.19 V, along with a J_{SC} of 15.1 mA/cm^2 and FF of 83.1%. The 2.19 V V_{OC} represents a significant improvement over the previous highest reported V_{OC} among the best all-perovskite tandems (2.05 V),[10,41–44] due to the high V_{OC} of the PDA-treated WBG subcell. We sent a tandem cell to an accredited independent PV calibration laboratory (NREL). The device delivered a certified PCE of 26.29% and V_{OC} of 2.13 V (Fig. 4e, Supplementary Fig. S23), and is the first certified all-perovskite tandem to surpass the record PCE (25.7%) of single-junction perovskite solar cells using the same asymptotic P_{max} (maximum power) scan protocol.[11,45] We also fabricated 1 cm^2 all-perovskite tandem solar cells, which delivered a PCE of 26.03% and V_{OC} of 2.16 V (Supplementary Fig. S24). We note that there is still room for improvement, particularly in the J_{SC} of the tandem as J_{SC} values of > 16.5 mA/cm^2 have been reported.[10] Therefore, we anticipate that PCEs approaching 30% are already experimentally feasible.

We tested operating stability using MPP tracking of an encapsulated tandem in ambient air (Fig. 4f). Under AM1.5G 1 sun illumination at the maximum power point, the device retained 86% of its initial PCE after 500 hours of continuous operation. This promising operating stability in combination with high V_{OC} and PCE enabled by diammonium surface modification represents an important step towards the application of all-perovskite tandem solar cells.

References:

1. Oliver, R. D. J. et al. Understanding and suppressing non-radiative losses in methylammonium-free wide-bandgap perovskite solar cells. *Energy Environ. Sci*. **15**, 714–726 (2022).

2. Mahesh, S. et al. Revealing the origin of voltage loss in mixed-halide perovskite solar cells. *Energy Environ. Sci*. **13**, 258–267 (2020).

3. Stranks, S. D., Hoye, R. L. Z., Di, D., Friend, R. H. & Deschler, F. The physics of light emission in halide perovskite devices. *Adv. Mater*. **31**, 1803336 (2019).

4. Stolterfoht, M. et al. Visualization and suppression of interfacial recombination for high-efficiency large-area pin perovskite solar cells. *Nat. Energy* **3**, 847–854 (2018).

5. Warby, J. et al. Understanding performance limiting interfacial recombination in pin perovskite solar cells. *Adv. Energy Mater*. **12**, 2103567 (2022).

6. Wang, R. et al. Prospects for metal halide perovskite-based tandem solar cells. *Nat. Photonics* **15**, 411–425 (2021).

7. Leijtens, T., Bush, K. A., Prasanna, R. & McGehee, M. D. Opportunities and challenges for tandem solar cells using metal halide perovskite semiconductors. *Nat. Energy* **3**, 828–838 (2018).

8. Al-Ashouri, A. et al. Monolithic perovskite/silicon tandem solar cell with >29% efficiency by enhanced hole extraction. *Science* **370**, 1300–1309 (2020).

9. Chen, W. et al. Monolithic perovskite/organic tandem solar cells with 23.6% efficiency enabled by reduced voltage losses and optimized interconnecting layer. *Nat. Energy* **7**, 229–237 (2022).

10. Lin, R. et al. All-perovskite tandem solar cells with improved grain surface passivation. *Nature* **603**, 73–78 (2022).

11. Best Research-Cell Efficiency Chart | Photovoltaic Research | NREL, (available at https://www.nrel.gov/pv/cell-efficiency.html).

12. Jeong, M. et al. Stable perovskite solar cells with efficiency exceeding 24.8% and 0.3-V voltage loss. *Science* **369**, 1615–1620 (2020).

13. Zhang, J. et al. Intermediate phase enhances inorganic perovskite and metal oxide interface for efficient photovoltaics. *Joule* **4**, 222–234 (2020).

14. Liu, Z., Siekmann, J., Klingebiel, B., Rau, U. & Kirchartz, T. Interface optimization via fullerene blends enables open-circuit voltages of 1.35 V in $CH_3NH_3Pb(I_{0.8}Br_{0.2})_3$ solar cells. *Adv. Energy Mater*. **11**, 2003386 (2021).

15. Tong, J. et al. Wide-bandgap metal halide perovskites for tandem solar cells. *ACS Energy Lett*. **6**, 232–248 (2021).

16. Stolterfoht, M. et al. The impact of energy alignment and interfacial recombination on the internal and external open-circuit voltage of perovskite solar cells. *Energy Environ. Sci*. **12**, 2778–2788 (2019).

17. Zhao, T., Chueh, C. C., Chen, Q., Rajagopal, A. & Jen, A. K. Y. Defect passivation of organic-inorganic hybrid perovskites by diammonium iodide toward high-performance photovoltaic devices. *ACS Energy Lett*. **1**, 757–763 (2016).

18. Ross, R. T. Some thermodynamics of photochemical systems. *J. Chem. Phys*. **46**, 4590 (2004).

19. Teale, S. et al. Dimensional mixing increases the efficiency of 2D/3D perovskite solar cells. *J. Phys. Chem. Lett*. **11**, 5115–5119 (2020).

20. Yang, S. et al. Stabilizing halide perovskite surfaces for solar cell operation with wide-bandgap lead oxysalts. *Science* **365**, 473–478 (2019).

21. Jiang, Q. et al. Surface passivation of perovskite film for efficient solar cells. *Nat. Photonics* **13**, 460–466 (2019).

22. Chen, H. et al. Quantum-size-tuned heterostructures enable efficient and stable inverted perovskite solar cells. *Nat. Photonics* **16**, 352–358 (2022).

23. Aber, A. G., Glunz, S. & Warta, W. Field effect passivation of high efficiency silicon solar cells. *Sol. Energy Mater. Sol. Cells*. **29**, 175–182 (1993).

24. Jang, Y. W. et al. Intact 2D/3D halide junction perovskite solar cells via solid-phase in-plane growth. *Nat. Energy* **6**, 63–71 (2021).

25. Wu, W.Q. et al. Bilateral alkylamine for suppressing charge recombination and improving stability in blade-coated perovskite solar cells. *Sci. Adv*. **5** 1-9 (2019).

26. Kapil, G. et al. Tin-lead perovskite fabricated via ethylenediamine interlayer guides to the solar cell efficiency of 21.74%. *Adv. Energy Mater*. **11**, 2101069 (2021).

27. Hu, S. et al. Optimized carrier extraction at interfaces for 23.6% efficient tin–lead perovskite solar cells. *Energy Environ. Sci*. **15**, 2096–2107 (2022).

28. Frohna, K. et al. Nanoscale chemical heterogeneity dominates the optoelectronic response of alloyed perovskite solar cells. *Nat. Nanotechnol*. **17**, 190–196 (2021).

29. Baldo, M. A, & Forrest, S. R. Interface-limited injection in amorphous organic semiconductors. *Phys. Rev. B*. **64**, 085201 (2001).

30. Saidaminov, M. I. et al. Multi-cation perovskites prevent carrier reflection from grain surfaces. *Nat. Mater*. **19**, 412–418 (2020).

31. Li, Z. et al. Organometallic-functionalized interfaces for highly efficient inverted perovskite solar cells. *Science* **376**, 416–420 (2022).

248 32. Zhang, F. et al. Metastable Dion-Jacobson 2D structure enables efficient and stable perovskite solar
249 cells. *Science* **375**, 71–76 (2022).

250 33. Zhang, L. et al. Surface defect passivation of pb–sn-alloyed perovskite film by 1,3-propanediammonium
251 iodide toward high-performance photovoltaic devices. *Sol. RRL*. **5**, 2100299 (2021).

252 34. Zhang, F. et al. Surface lattice engineering through three-dimensional lead iodide perovskitoid for high-
253 performance perovskite solar cells. *Chem* **7**, 774–785 (2021).

254 35. Park, B. et al. Understanding how excess lead iodide precursor improves halide perovskite solar cell
255 performance. *Nat. Commun*. **9**, 1–8 (2018).

256 36. Yan, N. et al. Ligand-Anchoring-Induced Oriented Crystal Growth for High-Efficiency Lead-Tin
257 Perovskite Solar Cells. *Adv. Funct. Mater*. **32**, 2201384 (2022).

258 37. Chiara, R. et al. The templating effect of diammonium cations on the structural and optical properties
259 of lead bromide perovskites: a guide to design broad light emitters. *J. Mater. Chem. C.* **10**, 12367 (2022).

260 38. Eperon, G. E. et al. Formamidinium lead trihalide: a broadly tunable perovskite for efficient planar
261 heterojunction solar cells. *Energy Environ. Sci*. **7**, 982–988 (2014).

262 39. Zheng, X. et al. Defect passivation in hybrid perovskite solar cells using quaternary ammonium halide
263 anions and cations. *Nat. Energy* **2**, 1–9 (2017).

264 40. Stolterfoht, M. et al. How to quantify the efficiency potential of neat perovskite films: perovskite
265 semiconductors with an implied efficiency exceeding 28%. *Adv. Mater*. **32**, 2000080 (2020).

266 41. Tong, J. et al. Carrier lifetimes of >1 ms in Sn-Pb perovskites enable efficient all-perovskite tandem
267 solar cells. *Science* **364**, 475–479 (2019).

268 42. Lin, R. et al. Monolithic all-perovskite tandem solar cells with 24.8% efficiency exploiting
269 comproportionation to suppress Sn(ii) oxidation in precursor ink. *Nat. Energy* **4**, 864–873 (2019).

43. Xiao, K. et al. All-perovskite tandem solar cells with 24.2% certified efficiency and area over 1 cm2 using surface-anchoring zwitterionic antioxidant. *Nat. Energy* **5**, 870–880 (2020).

44. Wen, J. et al. Steric Engineering Enables Efficient and Photostable Wide-Bandgap Perovskites for All-Perovskite Tandem Solar Cells. *Adv. Mater.* 2110356 (2022).

45. Song, T., Freidman, D.J. & Kopidakis, N. How Useful are Conventional I–Vs for Performance Calibration of Single- and Two-Junction Perovskite Solar Cells? A Statistical Analysis of Performance Data on ≈200 Cells from 30 Global Sources. *Sol. RRL*. **6**, 2100867 (2022).

Fig. 1 | Recombination between perovskite and ETL: analysis and strategies for its minimization. (**a**) Schematic crystal structure of the perovskite surface being treated with a PDA ligand. (**b**) PLQY data from control, butylammonium (BA) and propane diammonium (PDA) treated films with and without C_{60}, on an ITO/HTL substrate. (**c**) Band alignment of control and BA and PDA treated films compared with C_{60} (values from UPS/IPES measurements in Supplementary Fig. S2). (**d**) Work function difference (ΔW), between an untreated and PDA treated Pb-I terminated surface with a bromide vacancy (V_{Br}), is obtained by calculating electrostatic potential difference via $\Delta W = \Delta P = P_{untreated} - P_{treated}$. As a result, a positive value for ΔW represents a Fermi level upshift and a negative value for ΔW represents a Fermi level downshift. (**e**) Density of states (DOS) calculated for bulk perovskite and different surface structures. The detailed DOS plots in the gap region are shown in the zoomed-in insets. In each inset, the control (slab) DOS are represented as blue dashed lines.

Fig. 2 | Surface inhomogeneity and its remediation using surface-adsorbed molecular layers. (**a**) QFLS maps of control and PDA treated films demonstrating increased homogeneity and resistance to C_{60}-induced defects. (**b**) Histogram of QFLS pixel values taken from larger 100 µm x 100 µm images (Supplementary Fig. S10). KPFM images of (**c**) control and (**d**) PDA treated films. GIWAXS patterns of (**e**) control, (**f**) PDA treated films at 0.15° incident angle – the red circle draws the eye to obvious splitting of the (1 1 0) perovskite peak. Azimuthal integrations comparing surface (0.15°) and bulk (1.0°) crystal structures for (**g**) control and (**h**) PDA treated films. Transient reflection measurements of (**i**) control and (**j**) treated films. Films were encapsulated between two glass slides to mitigate environmental damage.

Fig. 3 | Characterization of WBG perovskite solar cells. (a) *J-V* curves of control and PDA treated WBG devices. (**b**) NREL-certified *J-V* curve of PDA-treated WBG perovskite solar cell. Devices were encapsulated to mitigate environmental damage. (**c**) PV parameters of control and treated devices (30 devices for each type). (**d**) Loss analysis for the PCE and V_{OC} of control and treated devices. PCE and V_{OC} losses were extracted from pseudo-*JV* measurements shown in Supplementary Fig. S18 and Supplementary Table S3.

Fig. 4 | PV Performance and stability of perovskite tandem solar cells (**a**) Schematic diagram of tandem device structure. (**b**) Cross-sectional SEM image of tandem device. (**c**) EQE curves of the WBG and NBG subcells within the tandem device and (**d**) *J-V* curves of champion NBG, WBG and all-perovskite tandem devices. (**e**) NREL-certified *J-V* curve of all-perovskite tandem device (Supplementary Fig. S23). (**f**) MPP

stability tracking of encapsulated WBG and tandem devices in ambient conditions under simulated 1 sun illumination (initial PCE of 19.0% and 26.9% respectively). The tandem device retains >86% of initial efficiency after 500 hours of operation.

Methods:

Materials

All materials were used as received without further purification. Commercial ITO substrates (20 Ω/sq) with 25 mm x 25 mm dimension were purchased from TFD Inc. The organic halide salts (FAI, FABr, MAI, BAI) as well as 4-Fluorophenethylammonium bromide (4F-PEABr) were purchased from GreatCell Solar Materials (Australia). Poly(3,4-ethylenedioxythiophene) polystyrene sulfonate (PEDOT: PSS) aqueous solution (Al 4083) was purchased from Heraeus Clevios (Germany). PbI_2 (99.99%), $PbBr_2$ (99.999%), CsBr (>99.0%) and [4-(3,6-Dimethyl-9H-carbazol-9-yl)butyl]phosphonic Acid (Me-4PACz) were purchased from TCI Chemicals. CsI (99.999%), SnI_2 (99.99%), SnF_2 (99%), Glycine hydrochloride (99%), Guanidine thiocyanate (GuaSCN, 99%), and ethane-1,2-diammonium iodide (EDAI2, 98%) were purchased from Sigma-Aldrich. C_{60}, Bathocuproine (BCP), $PDAI_2$ were purchased from Xi'an Polymer Light Technology (China). All the solvents used in the process were anhydrous and purchased from Sigma-Aldrich.

Perovskite precursor solutions

Wide bandgap perovskite. 1.2 M wide-band gap perovskite precursor solution with a composition of $FA_{0.8}Cs_{0.2}Pb(I_{0.6}Br_{0.4})_3$ was prepared by dissolving CsI, FAI, $PbBr_2$ and PbI_2 in mixed solvents of DMF and DMSO with a volume ratio of 4:1. The precursor solution was stirred at 60 ºC for 1 h and then filtered using a 0.22 μm PTFE membrane before use.

Narrow bandgap perovskite. 1.8 M narrow-bandgap perovskite precursor solution with a composition of $Cs_{0.05}FA_{0.7}MA_{0.25}Pb_{0.5}Sn_{0.5}I_3$ was prepared by dissolving CsI, FAI, MAI, SnI_2 and PbI_2 in the mixed solvents of DMF and DMSO with a volume ratio of 3:1. Tin powders (5 mg), GuaSCN (4 mg), SnF_2 (14 mg), 4F-

PEABr (2 mg) and glycine hydrochloride (4 mg) were added to the precursor solution. The precursor solution was then stirred at room temperature for 1 h. The precursor solution was filtered using a 0.22 μm Polytetrafluoroethylene (PTFE) membrane before using.

Solar cell fabrication

Single junction wide bandgap perovskite solar cells. NiO_x nanocrystal (10 mg ml^{-1} in H_2O and 2-Propanol mixed solvent with volume ratio of 3:1) layers were first spin-coated on ITO substrates at 3,000 rpm for 25 s in air without any post-treatment, then the substrates were immediately transferred to the glovebox. The NiO_x nanoparticles were prepared via the hydrolysis reaction of nickel nitrate referring to our previous work.[46] Me-4PACz (0.3 mg ml^{-1}) in ethanol was spin-coated on the NiO_x film at 3,000 rpm for 25 s and then annealed at 100 ºC for 10 min. For the perovskite film fabrication, the substrate was spun at 4000 rpm for 32 s with an acceleration of 1000 rpm, 100 μL Anisole was dropped onto the substrate during the last 8 s of the spinning. The substrates were then transferred onto a hotplate and heated at 100 °C for 15 min. The organic salts surface treatment solutions were prepared by dissolving $PDAI_2$, and BAI in IPA with different concentrations. The optimal concentration of $PDAI_2$ used in devices was 1 mg/ml. The surface treatment was finished by depositing 130 μl organic salts solution onto the perovskite film surface at a spin rate of 4,000 rpm for 25 seconds with a 1,000 rpm/s acceleration. The film was then annealed at 100 °C for 5 min. After cooling down to room temperature, the substrates were transferred to the evaporation system and a 20-nm-thick C_{60} film was subsequently deposited on top by thermal evaporation at a rate of 0.2 A s^{-1}. The substrates were then transferred to the atomic layer deposition (ALD) system (Picosun) to deposit 20 nm SnO_2 at 90 ºC using precursors of tetrakis(dimethylamino) tin (iv) (99.9999%) and deionized water. A 140 nm Ag electrode was then deposited by thermal evaporation.

Single junction Pb–Sn perovskite solar cells. The prepatterned indium tin oxide (ITO) glass substrates were sequentially cleaned using acetone and isopropanol. PEDOT: PSS was spin-coated on ITO substrates at 6,000 rpm for 30 s and annealed on a hotplate at 160 °C for 20 min in ambient air. After cooling, we

transferred the substrates immediately to a nitrogen-filled glovebox for the deposition of perovskite films. The perovskite films were deposited with a two-step spin-coating procedure: (1) 1,000 rpm for 10 s with an acceleration of 200 rpm s^{-1}, (2) 3800 rpm for 45s with an acceleration of 1000 rpm s^{-1}, 300 µl CB was dropped onto the spinning substrate during the second spin-coating step at 20 s before the end of the procedure. The substrates were then treated on hotplate for 10 min at 100 ºC. Post-treatment with $EDAI_2$ was carried out by spin-coating a solution of 0.5 mg/ml $EDAI_2$ in 4:3 IPA:Toluene at 4000 rpm for 25 s, followed by annealing at 100 °C for 5 min. 20 nm C60, 8 nm BCP and 140 nm Ag were sequentially deposited on top of the perovskite layer by thermal evaporation.

All-perovskite tandem solar cells. The wide bandgap perovskite solar cell fabrication was completed as described above until the deposition of ALD SnO_2. After ALD deposition of SnO_2, 1 nm of Au was deposited by thermal evaporation. Next, PEDOT:PSS (diluted at a 1:2 volume ratio in IPA) was spin-coated onto the wide bandgap subcell at 4000 rpm for 30 s and annealed at 120 °C for 10 min. The substrates were then cooled and transferred to a N_2-filled glovebox for the deposition of the narrow bandgap subcell. The narrow bandgap perovskite precursor solution was spin-coated onto the substrates at 1000 rpm for 10 s followed by 3800 rpm for 45 s. 20 s before the end of the second step, 300 µL of chlorobenzene was dropped onto the substrate. The substrate was then annealed at 100 °C for 10 min. Post-treatment with EDA was carried out by spin-coating a solution of 0.5 mg/ml $EDAI_2$ in 4:3 IPA:Toluene at 4000 rpm for 25 s, followed by annealing at 100 °C for 5 min. Finally, C_{60} (30 nm), ALD SnO_2 (20 nm) and Ag (140 nm) were sequentially deposited as described earlier.

Device testing

The current density-voltage (*J-V*) characteristics were measured using a Keithley 2400 source meter under illumination from a solar simulator (Newport, Class A) with a light intensity of 100 S5 mW cm^{-2} (checked with a calibrated reference solar cell from Newport). *J-V* curves were measured in a nitrogen atmosphere with a scanning rate of 100 mVs^{-1} (voltage step of 10 mV and delay time of 200 ms). The active area was

determined by the aperture shade mask (0.049 cm^2 for small-area devices) placed in front of the solar cell. A spectral mismatch factor of 1 was used for all *J-V* measurements. For stabilised output measurements at maximum power point (MPP), the device testing chamber was left under ambient conditions. Solar cells were fixed at the MPP voltage, (determined from *J-V* sweeps in both scanning directions) and current output was tracked over time. EQE measurements were performed in ambient air using a QuantX-300 Quantum Efficiency Measurement System (Newport) with monochromatic light focused on the device pixel and a chopper frequency of 20 Hz. For tandem solar cells, EQE measurements were performed in ambient air and the bias illumination from bright LEDs with emission peaks of 850 and 450 nm were used for the measurements of the front and back subcells, respectively. No bias voltage was applied during the EQE measurements of the tandem solar cells.

Stability testing

Devices were placed in a homemade stability tracking station. For the single-junction devices, the illumination source was a white light LED with intensity calibrated to match 1-sun conditions. For tandem solar cells, an AM1.5G solar simulator illumination source (G2V sunbrick) with an intensity of 100 mW cm^{-2} was used. For room temperature tests (ISOS-L-1I), device chamber was sealed and supplied with continuous N_2 purging. MPP were tracked by a perturb and observe algorithm that updates the MPP point every 10s. Encapsulation was done by capping device with a glass slide, using UV-adhesive (Lumtec LT-U001) as sealant.

Grazing Incidence Wide-Angle X-ray Scattering (GIWAXS)

GIWAXS measurements were conducted at the BXDS (LE-wiggler) beamline of the Canadian Light Source (CLS) using X-ray with a wavelength of λ= 0.82 Å at a grazing incidence angle of either 0.15° or 1°, and an exposure time of 5 s. The GIXRD patterns were collected by a MarCCD 225 detector with a sample-detector distance of 430 mm, and were presented in q coordinates using the equation $q=4\pi\sin\theta/\lambda$, where θ is half of the diffraction angle. In the present GIXRD data, q has been calibrated by measuring the XRD

from a Lanthanum hexaboride reference sample. Images were calibrated using LaB6 and processed via the Nika software package [47] and the GIXSGUI MATLAB plug-in [48].

Drift-diffusion simulations

Simulations of perovskite solar cells were conducted in the heterojunction solar cell simulator SCAPS-1D, version 3.3.07.[49]

TA/TR Spectroscopy

Femtosecond laser pulses of 1,030 nm generated by a Yb:KGW laser at a 5 kHz repetition rate (Pharos (Light Conversion)), passed through an optical parametric amplifier (Orpheus (Light Conversion)) selected for 450 nm light. The beam passed through the parametric amplifier served as the pump pulse, whereas the probe pulse was generated by focusing the initial 1,030 nm pulse into a sapphire crystal, which resulted in a white-light continuum (Helios (Ultrafast)). With a temporal resolution of the system of ~250 fs, each time step meant delaying the probe pulse with respect to the pump, with time steps that increased exponentially. Every other pump pulse was blocked with a chopper to determine the change in optical density. After going through a grating spectrograph, the pulses were measured by means of a charge-coupled device (CCD) (Helios (Ultrafast)).

Intensity-dependent photoluminescence quantum yield (PLQY) measurements

The excitation source was an unfocused beam of a 442 nm c.w. diode laser. Photoluminescence was collected using an integrating sphere with a pre-calibrated fibre coupled to a spectrometer (Ocean Optics QE Pro) with an intensity of ~300 mW cm^{-2}. PLQY values were calculated by $PLQY = \frac{P_S}{P_{Ex*A}}$, where $A = 1 - \frac{P_L}{P_{Ex}}$, P_S is the integrated photon count of sample emission upon laser excitation; P_{Ex} is the integrated photon count of the excitation laser when the sample is removed from integrating sphere, and P_L is the integrated photon count of excitation laser when sample is mounted in the integrating sphere and hit by the beam. A set of neutral density filters were used to vary the excitation density.

TRPL spectroscopy

TRPL measurements were performed using a Horiba Fluorolog Time Correlated Single Photon Counting (TCSPC) system with photomultiplier tube detectors. A pulsed laser diode (532 nm, 110 – 140 ps pulse width) was used as excitation sources for steady-state and transient measurements. For transient measurements, a 160 ns period (0.28 nJ per pulse) was used to capture accurate lifetimes carrier lifetimes.

IPES and UPS

For combined ultraviolet photoelectron spectroscopy (UPS) and inverse photoelectron spectroscopy (IPES) measurements, an Excitech H Lyman-α photon source (10.2 eV) with an oxygen-filled beam path was used for excitation and coupled with a PHI 5600 ultrahigh vacuum system with a hemispherical electron energy analyzer. A sample bias of -5 V and a pass energy of 5.85 eV were used for UPS acquisition. Inverse photoelectron spectroscopy (IPES) measurements were performed in the Bremsstrahlung isochromat mode with electron kinetic energies below 5 eV and an emission current of 2 μA to minimize sample damage. A Kimball Physics ELG-2 electron gun with a BaO cathode was used to generate the electron beam and the emitted photons were collected with a bandpass photon detector that included an optical bandpass filter (280 nm for 3F-PEA and BA treated films, and 254 nm for control and PEA treated) and a photomultiplier tube (R585, Hamamatsu Photonics). Samples were held at a -20 V bias during all IPES measurements and the UHV chamber was blacked-out to exclude external light.

Perovskite films sent for combined UPS/IPES were fabricated on ITO/NiO_x/Me-4PACz substrates.

Transient photovoltage/photocurrent

These measurements were carried out according to reference [50].

Kelvin Probe Force Microscopy (KPFM)

Kelvin Probe Force Microscopy (KPFM) images were generated using an Asylum Cypher S atomic force microscope (Oxford Instruments; Asylum Research, Santa Barbara, USA) with a Ti-Ir coated

ASYELEC.01-R2 cantilever with k=4±0.5 N/m (Asylum Research). Scans were performed over 2 μm at 512 pixels and 0.5 Hz in a two-pass nap method; the first pass in tapping mode and the second in KPFM mode with a tip potential of 5V and surface clearance of 5 nm. Cantilever calibration was performed using the Asylum Research GetReal database.

Hyperspectral imaging

Perovskite films were deposited on HTL/ITO films using the same recipe as used for device fabrication, and the C_{60} film was evaporated on top of perovskite films to have *pin* device stack. The absolute PL spectra of the encapsulated samples were collected using a hyperspectral imaging system coupled to a microscope with 2 nm spectral resolution (Photon etc. IMA). Samples were excited from the top surface of perovskite (and C_{60} layer) with 405 nm laser at ~1 sun illumination condition.[51] The absolute calibration procedure of the setup is reported in detail elsewhere.[52] The collected data was analyzed via home-built MatLab code using modified Würfel's generalized Plank law to get quasi-Fermi level splitting (QFLS, Δμ):[53–56]

$$\varphi_{(E,\theta)} = A_{(E,\theta)} \frac{\cos\theta}{4\pi^3\hbar^3 c_0^2} E^2 \frac{1}{exp\left(\frac{E-\Delta\mu}{k_B T}\right) - 1}$$

where $A_{(E,\theta)}$ is the absorption probability of a photon with energy E, incident at an angle θ with respect to the surface normal. $k_B T$ is Boltzmann constant and the temperature (equivalent to 25.7 meV at room temperature). Here, $\cos\theta$ factor appears as the emission from the surface following the Lambert's law. Finally, fitting is applied to each data cube to construct the images with 2 pixel averaging, which gives spatial resolution ~ 0.6 μm/pixel.

SEM

High-resolution SEM images were obtained using the Hitachi S5200 microscope with an accelerating voltage of 1.5 kV. A low accelerating voltage and a low beam current were deployed to reduce surface damage of perovskite films under electron beam bombardment.

Pseudo-*JV* (*pJV*)

Pseudo-*JV* curves were plotted based on the intensity-dependent PLQY measurements. First, quasi-Fermi level splitting (QFLS) is calculated by the PLQY values at various excitation light intensities:

$$QFLS = k_B T \times ln(PLQY \times S \times J_G / J_{0,rad})$$

where S is the sun-equivalent excitation intensity, J_G the generated current density at 1 sun (taken from device J_{SC}) and $J_{0,rad}$ the radiative recombination current in the dark (taken from the dark current value from Shockley-Queisser limit).

Since the generated current density is proportional to the excitation light intensity, an exponential current–QFLS curve is created that ideally follows the same functional dependence on voltage as the dark current–voltage curve of a diode without any series resistance. Subtracting this from a charge generation current density at 1 sun (J_G) creates a *pJV* curve that is only limited by non-radiative recombination processes in the cell but not by the transport and/or the series resistances.

DFT Calculations

All DFT calculations were done by FHI-aims code.[57–59] The default numerical settings, referred to as "intermediate" in FHI-aims were used. Local minimum-energy geometries of Born-Oppenheimer surfaces were obtained with residual total energy gradients below $1x10^{-2}$ eV/ Å for atomic positions by the PBE-GGA functional[60] within the Van der Waals corrections followed by the Tkatcheko-Scheffler (TS)[61] method. The density of states (DOS) is calculated through PBE-GGA functional, including spin-orbit coupling effects[62] within a k-point grid of 2x2x1 to sample the Brillouin zone that corresponds to the unit cell shown in Supplementary Fig. S7 b,c.

To mimic the experimental compositions $Cs_{0.2}FA_{0.8}Pb(I_{0.6}Br_{0.4})_3$, an alloyed structure was first built by using a 2x2x2 supercell based on the cubic phase conventional cells (as shown in Supplementary Fig. S7 a) within a composition, $Cs_{0.25}FA_{0.75}Pb(I_{0.584}Br_{0.416})_3$. Next, the slab structures (as shown in Supplementary Fig. S7 b,c, the total c axis is set to 100 Å) were built based on these PBE+TS relaxed alloyed structures

in a 1x1x3 supercell for Pb-I terminated and (FA, Cs)-I terminated surfaces. The detailed surface configurations are very important for prediction of work function tunability, which will be largely affected by the surface terminations and surface defects. As a result, three different surface configurations (perfect surface, surface with one iodine vacancy V_I, and surface with one bromine vacancy V_{Br}) are considered for the Pb-I terminations. On the other hand, five different surface configurations (perfect surface, surface with one Cs vacancy V_{Cs}, surface with one FA vacancy V_{FA}, surface with one iodine vacancy V_I, and surface with one bromine vacancy V_{Br}) are considered for (FA, Cs)-I terminations. In all of the geometry relaxations for the slab, the bottom three layers of atoms are fixed to mimic the bulk environment, and the atomic positions of all the atoms besides these three layers are relaxed by PBE+TS.

Based on these relaxed slab structures, we can calculate the work function changes caused by PDA treatment according to the electrostatic potential difference between the treated surface (ligands on top, Supplementary Fig. S8 b (bottom)) and the untreated surface (Supplementary Fig. S8 b (top)) as shown in Supplementary Fig. S8 c. Among different surface configurations (Supplementary Fig. S8 a), the Pb-I terminated surface with the bromide vacancy V_{Br} provides the closest agreement of ΔW after PDA treatment (theoretically calculated value is 0.12 eV) with the experimental UPS data (experimental result is 0.1 eV, Fig. 1c). Next, the detailed density of states comparison is used to elucidate the possible changes to the surface states after PDA treatment and their corresponding n-doping/p-doping effects. In the DOS comparison plots, the contribution from the 3rd bottom fixed Pb-I layers in the slab (as shown in Supplementary Fig. S7 c) is used to align the DOS positions to the bulk case (as shown in Supplementary Fig. S9).

Additional References:

46. Chen, H. et al. Efficient and stable inverted perovskite solar cells incorporating secondary amines. *Adv. Mater*. **31**, 1903559 (2019).

519 47. Ilavsky, J. Nika: Software for two-dimensional data reduction. *J. Appl. Crystallogr*. **45**, 324–328 (2012).

520 48. Jiang, Z. GIXSGUI: A MATLAB toolbox for grazing-incidence X-ray scattering data visualization and
521 reduction, and indexing of buried three-dimensional periodic nanostructured films. *J. Appl. Crystallogr*. **48**,
522 917–926 (2015).

523 49. Burgelman, M., Nollet, P. & Degrave, S. Modelling polycrystalline semiconductor solar cells. *Thin*
524 *Solid Films* **361–362**, 527–532 (2000).

525 50. Shao, Y., Yuan, Y. & Huang, J. Correlation of energy disorder and open-circuit voltage in hybrid
526 perovskite solar cells. *Nat. Energy* **1**, 1–6 (2016).

527 51. Aydin, E. et al. Ligand-bridged charge extraction and enhanced quantum efficiency enable efficient n–
528 i–p perovskite/silicon tandem solar cells. *Energy Environ. Sci*. **14**, 4377–4390 (2021).

529 52. Delamarre, A., Lombez, L. & Guillemoles, J. F. Characterization of solar cells using
530 electroluminescence and photoluminescence hyperspectral images. *J. Photonics Energy* **2**, 027004 (2012).

531 53. Rau, U. Reciprocity relation between photovoltaic quantum efficiency and electroluminescent emission
532 of solar cells. *Phys. Rev. B Condens. Matter Mater. Phys.* **76**, 085303 (2007).

533 54. Beloborodov, A. M., Hascoët, R., Vurm, I. & Wurfel, P. The chemical potential of radiation. *J. Phys.*
534 *C. Solid State Phys*. **15**, 3967 (1982).

535 55. El-Hajje, G. et al. Quantification of spatial inhomogeneity in perovskite solar cells by hyperspectral
536 luminescence imaging. *Energy Environ. Sci*. **9**, 2286–2294 (2016).

537 56. Wurfel, P., Finkbeiner, S. & Daub, E. Generalized Planck's radiation law for luminescence via indirect
538 transitions. *Appl. Phys. A.* **60**, 67-70 (1995).

539 57. Ren, X. et al. Resolution-of-identity approach to Hartree–Fock, hybrid density functionals, RPA, MP2
540 and GW with numeric atom-centered orbital basis functions. *New J. Phys.* **14**, 053020 (2012).

58. Havu, V., Blum, V., Havu, P. & Scheffler, M. Efficient O(N) integration for all-electron electronic structure calculation using numeric basis functions. *J.Comput. Phys*. **228**, 8367–8379 (2009).

59. Blum, V. et al. Ab initio molecular simulations with numeric atom-centered orbitals. *Comput. Phys. Commun*. **180**, 2175–2196 (2009).

60. Perdew, J. P., Burke, K. & Ernzerhof, M. Generalized gradient approximation made simple. *Phys. Rev. Lett*. **77**, 3865 (1996).

61. Tkatchenko, A. & Scheffler, M. Accurate molecular van der Waals interactions from ground-state electron density and free-atom reference data. *Phys. Rev. Lett*. **102**, 073005 (2009).

62. Huhn, W. P. & Blum, V. One-hundred-three compound band-structure benchmark of post-self-consistent spin-orbit coupling treatments in density functional theory. *Phys. Rev. Mater*. **1**, 033803 (2017).

Data and Materials Availability:

All data are available in the main text or supplementary materials. The data and code that support the findings of this study are available from the corresponding authors on reasonable request.

Acknowledgements

The authors thank Dr. Jonathan Warby for a useful discussion that contributed to our understanding of perovskite/ETL interfaces and Tao Song and Nikos Kopidakis at NREL for device certification. Z.W. acknowledges the Banting Postdoctoral Fellowships Program of Canada. GIWAXS patterns were collected at the BXDS-WLE Beamline at the Canadian Light Source (CLS) with the assistance of Dr. Chang-Yong Kim and Dr. Adam Leontowich.

Funding: This research was made possible by the US Department of the Navy, Office of Naval Research Grant (N00014-20-1-2572 and N00014-20-1-2725), the U.S. Department of Energy's Office of Energy

Efficiency and Renewable Energy (EERE) under the Solar Energy Technologies Office Award Number DE-EE0008753. This work was supported in part by the Ontario Research Fund-Research Excellence program (ORF7-Ministry of Research and Innovation, Ontario Research Fund-Research Excellence Round 7). This work was also supported by the King Abdullah University of Science and Technology (KAUST) under Award No. OSR-CRG2020-4350. This work was authored in part by the National Renewable Energy Laboratory, operated by Alliance for Sustainable Energy, LLC , for the U.S. Department of Energy (DOE) under Contract No. DE-AC36-08GO28308. NREL authors acknowledge support from Operational Energy Capability Improvement Fund (OECIF) of the Department of Defense. The views expressed in the article do not necessarily represent the views of the DOE or the U.S. Government. The CLS is funded by NSERC, the Canadian Institutes of Health Research, CFI, the Government of Saskatchewan, Western Economic Diversification Canada, and the University of Saskatchewan. This work was also supported by the Natural Sciences and Engineering Council of Canada and the Vanier Canada Graduate Scholarship.

Author Contributions: H.C., A.M., S.T. and B.C. planned the experiments and coordinated the work. H.C. fabricated the wide bandgap devices and tandems for performance and certification and fabricated the perovskite films for characterizations. H.C., A.M., C.L. and L.C. fabricated the narrow bandgap devices and tandems. S.T. and A.M. wrote the original draft. S.T., B.C., E.U. and S.D.W. carried out optical spectroscopy of films and devices and did data analysis. T.Z. carried out DFT calculations. G.H. and S.D.W. carried out UPS measurements and data analysis. P.S. and T.F. carried out Kelvin probe force microscopy and data analysis. S.T. and L.G. carried out GIWAXS measurements and analysed the data. J.W., Z.W., L.Z., S.P. and L.G. helped optimize the single junction and tandem device structure. R.A.A. conducted the TAS measurements. X.Z., J.M.L., C.X., B.S., C.L., Y.Yang, M.G.K. and N.J.P. assisted with device analysis and data interpretation. E.H.S., Y.Yan, S.D.W. and M.G.K. secured funding and helped to review and edit the manuscript.

Competing Interests:

The authors declare no competing interests.

588 **Supplementary Materials**

589 Supplementary Notes

590 Supplementary Figs. S1 – S24

591 Supplementary Tables S1 – S4

592 References 63 – 72

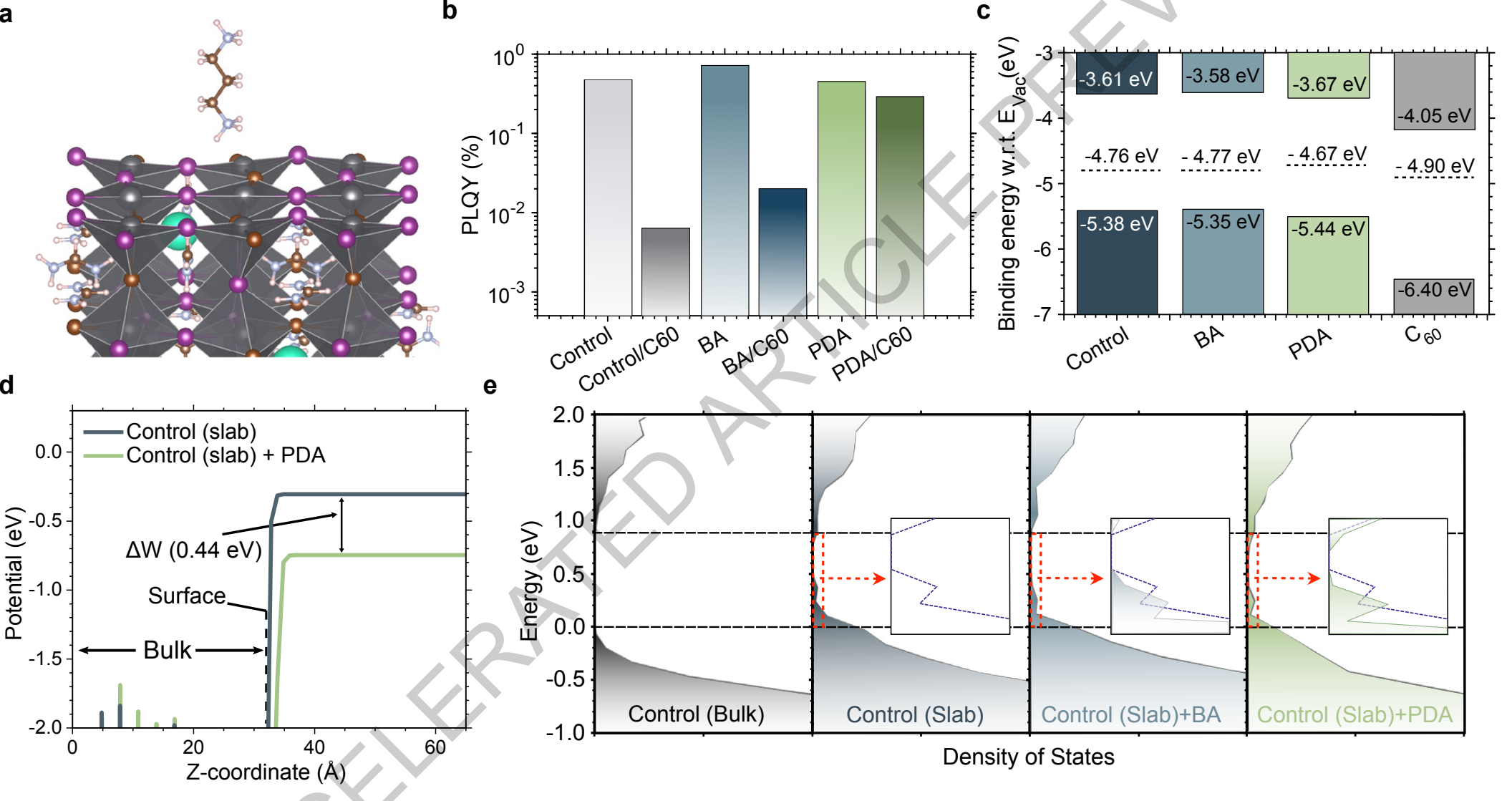

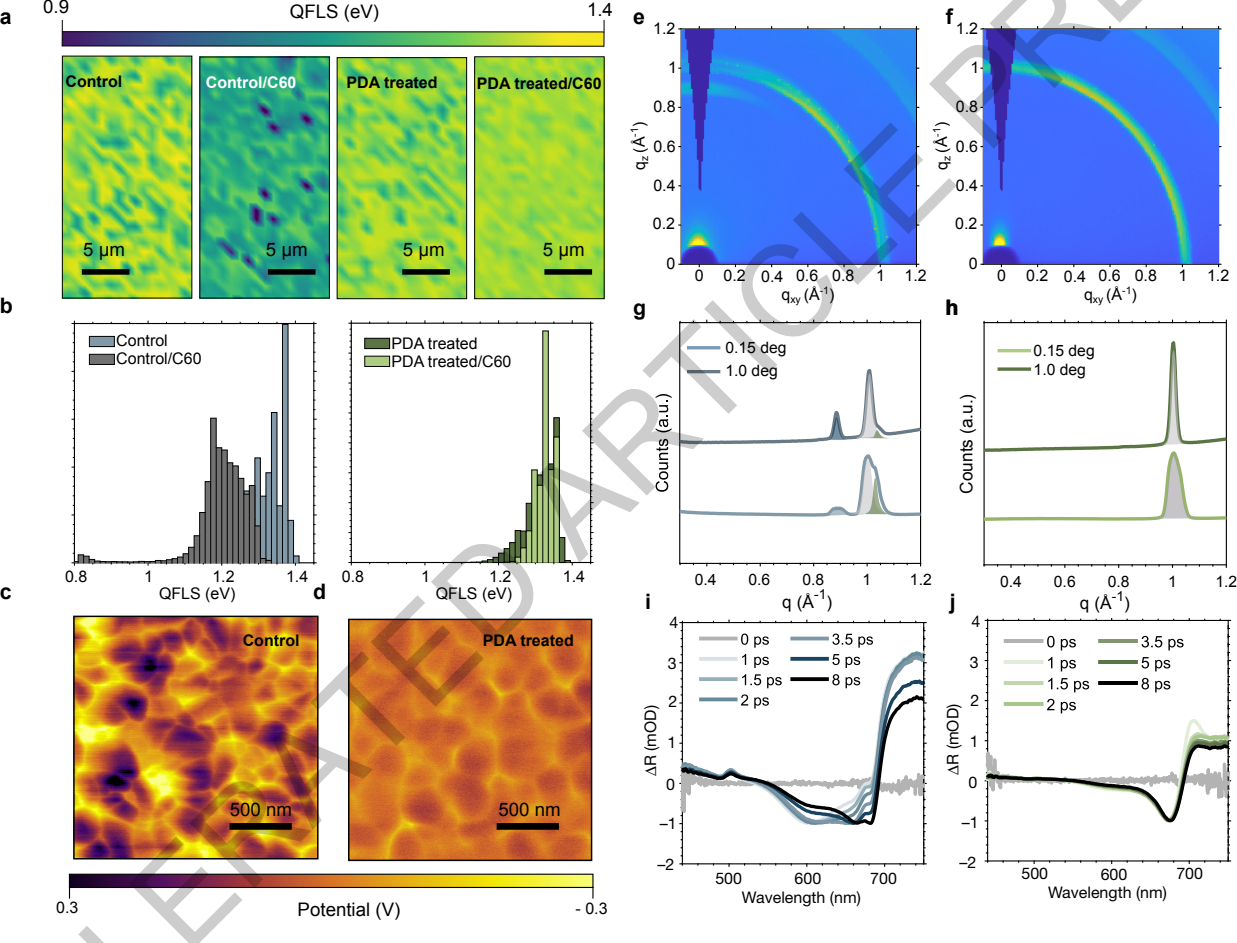

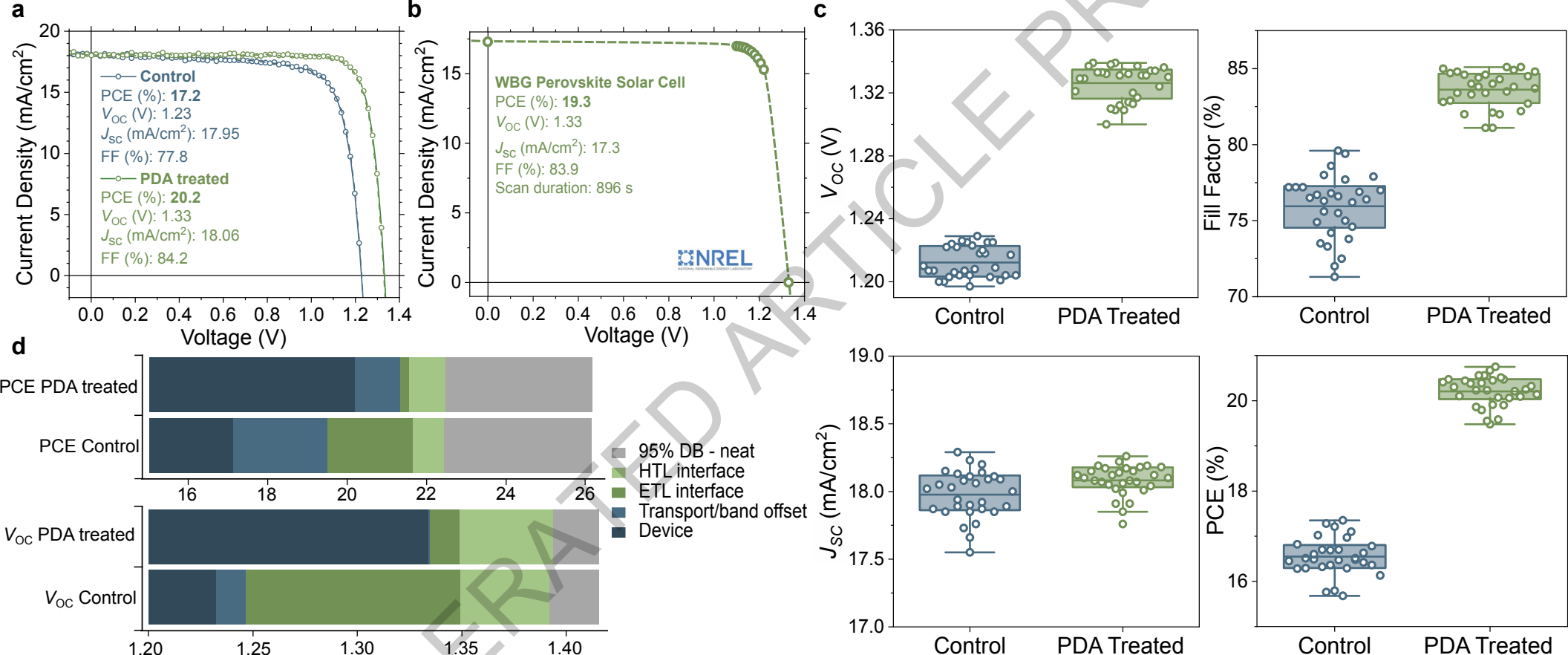
a
Current Density (mA/cm^2)
Voltage (V)
Control
PCE (%): 17.2
V_{OC} (V): 1.23
J_{sc} (mA/cm^2): 17.95
FF (%): 77.8
PDA treated
PCE (%): 20.2
V_{OC} (V): 1.33
J_{sc} (mA/cm^2): 18.06
FF (%): 84.2
b
WBG Perovskite Solar Cell
PCE (%): 19.3
V_{OC} (V): 1.33
J_{sc} (mA/cm^2): 17.3
FF (%): 83.9
Scan duration: 896 s
NREL
c
V_{OC} (V)
Fill Factor (%)
J_{SC} (mA/cm^2)
PCE (%)
Control
PDA Treated
d
PCE PDA treated
PCE Control
V_{OC} PDA treated
V_{OC} Control
95% DB - neat
HTL interface
ETL interface
Transport/band offset
Device

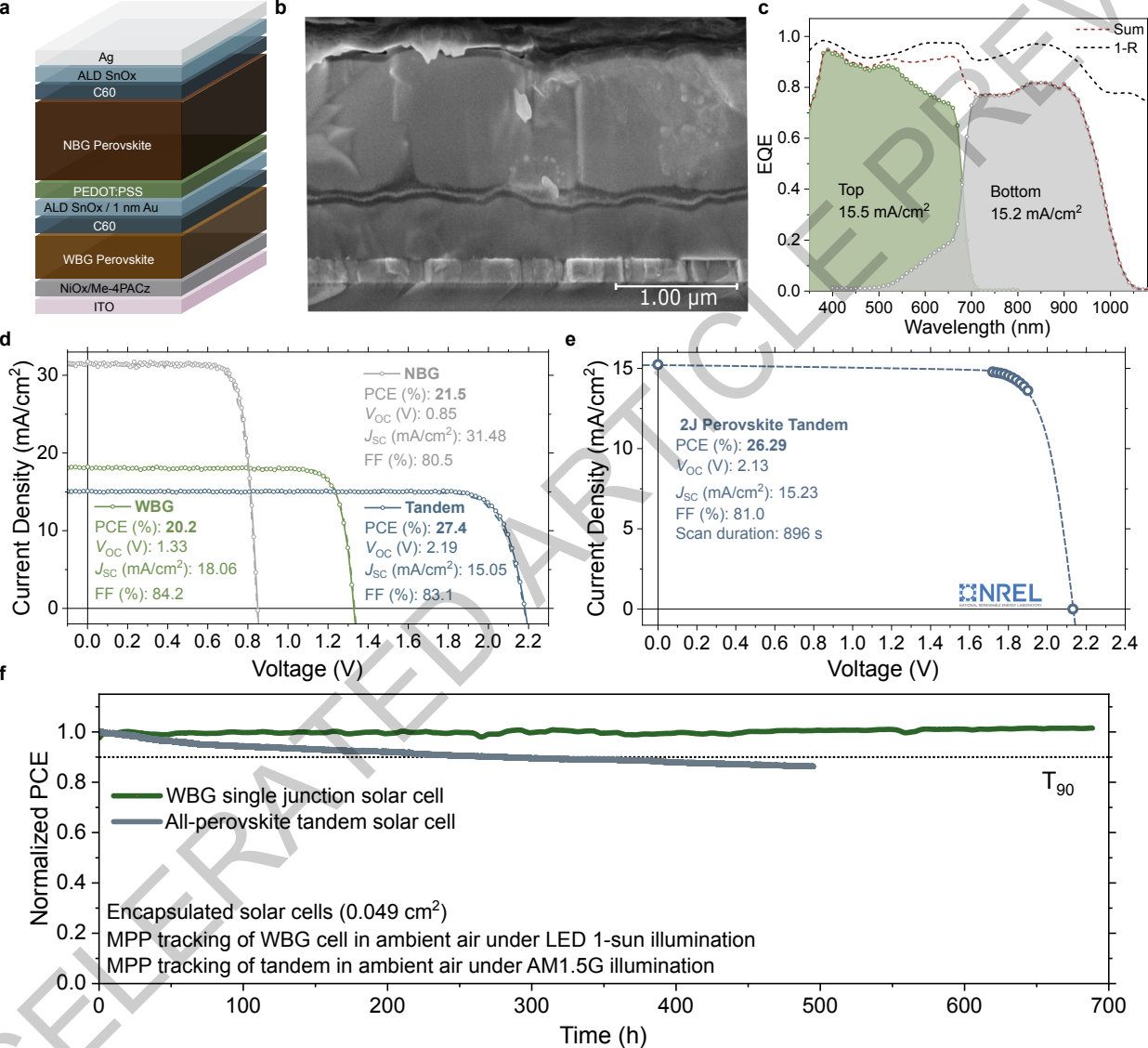

nature research

Corresponding author(s): Edward Sargent
Yanfa Yan

Solar Cells Reporting Summary

Nature Research wishes to improve the reproducibility of the work that we publish. This form is intended for publication with all accepted papers reporting the characterization of photovoltaic devices and provides structure for consistency and transparency in reporting. Some list items might not apply to an individual manuscript, but all fields must be completed for clarity.

For further information on Nature Research policies, including our data availability policy, see Authors & Referees.

Experimental design

Please check: are the following details reported in the manuscript?

1. Dimensions

Area of the tested solar cells	☒ Yes ☐ No	Device testing in Methods
Method used to determine the device area	☒ Yes ☐ No	Device testing in Methods

2. Current-voltage characterization

Current density-voltage (J-V) plots in both forward and backward direction	☒ Yes ☐ No	Figure 3a & 4d
Voltage scan conditions *For instance: scan direction, speed, dwell times*	☒ Yes ☐ No	Figure 3a,b & 4d,e
Test environment *For instance: characterization temperature, in air or in glove box*	☒ Yes ☐ No	Device testing in Methods
Protocol for preconditioning of the device before its characterization	☒ Yes ☐ No	Solar cell fabrication and device testing in Methods
Stability of the J-V characteristic *Verified with time evolution of the maximum power point or with the photocurrent at maximum power point; see ref. 7 for details.*	☒ Yes ☐ No	Stability testing in Methods, Figure 3b & Figure 4e

3. Hysteresis or any other unusual behaviour

Description of the unusual behaviour observed during the characterization	☐ Yes ☒ No	Negligible hysteresis
Related experimental data	☒ Yes ☐ No	Throughout main text and supplementary information

4. Efficiency

External quantum efficiency (EQE) or incident photons to current efficiency (IPCE)	☒ Yes ☐ No	Figure 4c, Figure S15
A comparison between the integrated response under the standard reference spectrum and the response measure under the simulator	☒ Yes ☐ No	Certified results in Fig. 3b, Fig. 4e, supplementary figs. 16, 23
For tandem solar cells, the bias illumination and bias voltage used for each subcell	☒ Yes ☐ No	Device testing in methods

5. Calibration

Light source and reference cell or sensor used for the characterization	☒ Yes ☐ No	Device testing in methods
Confirmation that the reference cell was calibrated and certified	☒ Yes ☐ No	Device testing in methods

Calculation of spectral mismatch between the reference cell and the devices under test	☒ Yes ☐ No	Device testing in methods

6. Mask/aperture

Size of the mask/aperture used during testing	☒ Yes ☐ No	Device testing in methods
Variation of the measured short-circuit current density with the mask/aperture area	☒ Yes ☐ No	Figure S16, S17, S23, S24

7. Performance certification

Identity of the independent certification laboratory that confirmed the photovoltaic performance	☒ Yes ☐ No	Main text, Figure 3b & 4e, Fig. S16, S23
A copy of any certificate(s) *Provide in Supplementary Information*	☒ Yes ☐ No	Fig S16, S23

8. Statistics

Number of solar cells tested	☒ Yes ☐ No	Fig 3c
Statistical analysis of the device performance	☒ Yes ☐ No	Fig 3c

9. Long-term stability analysis

Type of analysis, bias conditions and environmental conditions *For instance: illumination type, temperature, atmosphere humidity, encapsulation method, preconditioning temperature*	☒ Yes ☐ No	Fig 4f, stability testing in methods